CORA Cork Open Research Archive
Cartlann Taighde Oscailte Chorcaí

Title	Electromagnetic energy harvesting based on HfZrO tunneling junctions
Authors	Modreanu, Mircea;Dragoman, Mircea;Povey, Ian M.;Aldrigo, Martino;Dinescu, Adrian;Dragoman, Daniela
Publication date	2018-08-31
Original Citation	Dragoman, M. L., Modreanu, M., Povey, I. M., Aldrigo, M., Dinescu, A. and Dragoman, D. (2018) 'Electromagnetic energy harvesting based on HfZrO tunneling junctions', Nanotechnology, 29(44), 445203 (7pp). doi:10.1088/1361-6528/aada6a
Type of publication	Article (peer-reviewed)
Link to publisher's version	10.1088/1361-6528/aada6a
Rights	© 2018, IOP Publishing. All rights reserved. Reproduced by permission of the publisher. This is an author-created, un-copyedited version of an article published in Nanotechnology. IOP Publishing Ltd is not responsible for any errors or omissions in this version of the manuscript or any version derived from it. The Version of Record is available online at 10.1088/1361-6528/aada6a
Download date	2026-10-12 05:40:09
Item downloaded from	https://hdl.handle.net/10468/6732

UCC
University College Cork, Ireland
Coláiste na hOllscoile Corcaigh

ELECTROMAGNETIC ENERGY HARVESTING BASED ON HfZrO TUNNELING JUNCTIONS

Mircea Dragoman[1*], Mircea Modreanu[2], Ian M. Povey[2], Martino Aldrigo[1], Adrian Dinescu[1], Daniela Dragoman[3,4]

[1]National Institute for Research and Development in Microtechnologies (IMT Bucharest), Erou Iancu Nicolae Street 126A, 077190 Voluntari (Ilfov), Romania,

[2]Tyndall National Institute-University College Cork, Lee Maltings Complex, Dyke Parade, Cork, Ireland

[3]Univ. Bucharest, Physics Faculty, P.O. Box MG-11, 077125 Bucharest, Romania

[4]Academy of Romanian Scientists, Splaiul Independentei 54, 050094 Bucharest, Romania

Abstract

HfZrO ferroelectrics with a thickness of 6 nm were grown directly on Si using atomic layer deposition, top and bottom metallic electrodes being subsequently deposited by electron-beam metallization techniques. Depending on the polarity of the ±10 V poling voltages, the current-voltage dependence of these tunneling diodes shows a rectifying behavior for different polarizations, the ON-OFF ratio being about 10^4. Because the currents are at mA level, the HfZrO tunneling diodes coupled to an antenna array can harvest electromagnetic energy at 26 GHz (a bandwidth designated for Internet of Things-IoT), with a responsivity of 63 V/W and a NEP of 4 nW/Hz$^{0.5}$.

---

*Corresponding author. Email: mircea.dragoman@imt.ro

1. Introduction

Ferroelectric HfZrO (HfO_2 doped with Zr, or $Hf_xZr_{1-x}O_2$) was discovered a few years ago, when doping HfO_2 with a range of dopants, including Zr. There is extensive experimental evidence regarding the occurrence of the orthorhombic crystalline structure in HfZrO, which supports ferroelectric behavior [1,2]. Because HfZrO is the first ferroelectric material that is CMOS-compatible at the large wafer scale, many applications have been envisaged in recent years. For instance, in the context of negative capacitance induced by ferroelectrics, HfZrO field-effect transistors (FETs) in a back-gated configuration were shown to reduce the subthreshold swing below 60 mV/decade at room temperature [3] for a device with a channel consisting of flakes of MoS_2 monolayers, or Si in the case of FinFETs [4]. The negative capacitance is also promising for differential amplification without an external energy source due to polarization switching of the ferroelectric and energy transfer to the dielectric capacitor [5]. On the other hand, microwave applications of HfZrO have emerged, relying on the extraordinary tunability of microwave devices at few volts [6], such as wafer-scale phase shifters based on a 6 nm thick HfZrO ferroelectric grown directly on a high-resistivity silicon substrate, which shows 60^o phase shift at 1 GHz when the DC voltage is swept in the range ±3 V [7]. Furthermore, an integrated phase antenna array on HfZrO working at 2.55 GHz was developed, formed from two patched antennas, which steer the radiation beam with 25° when the DC voltage is swept within ±1 V [8].

Ferroelectric tunneling junctions (FTJ) [9] are in fact metal-insulator-metal (MIM) diodes where the ferroelectric is a few nanometers thick. However, in contrast to MIM diodes (for a review see [10]), the current of FTJs at a certain bias can be switched ON and OFF by the poling voltages, which switch the orientation of ferroelectric domains. On the other hand, these nanodevices are based on very thin ferroelectric layers, in the range of 1-3 nm, and the metallic contact is a problem for tunneling in terms of roughness, so that very often conductive AFM tips replace metallic electrodes. In addition, the ferroelectric materials for FTJs and the substrates on which they are grown, such as: $BaTiO_3/La_{0.67}Sr_{0.33}MnO_3$ (BTO/LSMO) [11], $Sm_{0.1}Bi0_{.9}FeO_3$/

Nb:$SrTiO_3$ (SBFO/NSTO) [12], or Pt/BTO/NSTO [13], are not easily integrable in CMOS technology. This is a major disadvantage, since CMOS technology is the only one able to integrate billions of devices on a single chip. In this context, the interest in HfZrO ferroelectric is very high, not only because it is compatible with CMOS technology, but also thanks to its physical properties, such as the dependence of permittivity on the applied voltage, hysteretic current-voltage and/or capacitance-voltage characteristics, and negative capacitance, which are not currently encountered in integrated CMOS devices.

There are many tunneling devices that can be integrated in CMOS technology, but the MIM configuration is the simplest, MIM devices being the only electronic devices able to work up to infrared [14]. The ferroelectric MIM (FTJ) allows, in addition, the control of the tunneling transport, i.e. ON and OFF switching, via DC poling signals. The aim of this paper is thus to show that even in thicker HfZrO ferroelectric layers (6 nm), which are part of a metal-ferroelectric-semiconductor (MFS) configuration, the charge transport mechanism is still based on tunneling, and can be controlled by electric poling signals. This finding can be used for harvesting the electromagnetic energy at 26 GHz when HfZrO tunneling diodes are coupled to an antenna array, in order to feed, for instance, connected devices in an IoT network.

2. Fabrication and characterization of tunneling HfZrO devices

We have grown 6-nm-thick $Hf_xZr_{1-x}O_2$ layers by atomic layer deposition (ALD), using a Cambridge NanoTech F200 reactor at 250 ^oC, on a *p*-doped Si(100) substrate. The following precursors were involved: Tetrakis(ethylmethyl-amido) hafnium (TEMAHf), Tetrakis(ethyl-methyl-amido) zirconium (TEMAZr), and water. Both metal precursors have the same nominal growth rate, of 0.1 nm per cycle, 30 super-cycles of [TEMAHf /H_2O/TEMAZr/H_2O] being employed to generate a well-mixed near 50:50 Hf:Zr composition. Nucleation delays and metal segregation are assumed to be absent. We have to point out that ALD growth of $Hf_{0.45}Zr_{0.55}O_{1.76}$ on Si is a very effective method to passivate the Si surface without producing additional defects,

thus avoiding the formation of large space-charge regions and surface channels, because of the formation of a SiO_x interlayer between HfZrO and Si during growth [15,16].

The film thickness, measured by spectroscopic ellipsometry (Woollam M2000), was found to be 5.8±0.2 nm with the help of a four layer optical model: air/$Hf_xZr_{1-x}O_2$/SiO_2/Si [17]. The chemical composition of the HfZrO films, namely $Hf_{0.45}Zr_{0.55}O_{1.76}$, was determined by X-ray photoelectron spectroscopy (XPS) using a Kratos AXIS ULTRA spectrometer with a source of monochromatic Al K_α, of 1486.58 eV. Further details about XPS characterization and grazing incidence X-ray diffraction patterns, which reveal the ferroelectric, orthorhombic phase with Pbc21 symmetry of our samples can be found in Ref. 18.

To better evidence the ferroelectric behavior of HfZrO thin films, Piezoelectric Force Microscopy (PFM) experimental data were obtained using the NT-MDT Solver Pro P-47 AFM. Measurements were performed in piezoresponse force mode by using a low-stiffness conductive probe (Pt-coated tip with a spring constant of 0.003-0.13 N/m (Tips Nano, CSG01/Pt)). Height and phase images were acquired by using 256×256 (x,y) positions (pixels). The ferroelectric property of the $Hf_{0.45}Zr_{0.55}O_{1.76}$ thin film has been assessed by piezoresponse force mode by applying a bias between the conductive tip and the sample. The images reported in Figs. 1(a) and 1(b) show the surface morphology and the phase, respectively, while a bias was alternated between +2/-2 V. As already observed by other authors [19,20], the PFM phase image shows a stripe domains structure induced by an electrically biased scanning tip, while the corresponding topography, before applying bias, is characterized by a flat structure.

In PFM measurements, the ferroelectric behavior is highlighted by the distinct dark and bright contrast areas that appear as a function of the applied bias. Indeed, during the acquisition of the images the probe operates by oscillating at a frequency that is close to the characteristic frequency of the system cantilever-probe-sample, such that the oscillations of the cantilever in contact with the sample are resonant. Accordingly, the oscillation phase will be different for

those domains of the $Hf_{0.45}Zr_{0.55}O_{1.76}$ film with different orientation of the polarization vector. For further information on the PFM studies, see [18].

After the $Hf_{0.45}Zr_{0.55}O_{1.76}$ oxide was grown and characterized, top and bottom electrodes were deposited using the e-beam evaporation system Temescal FC200. The top electrodes are Cr (5 nm)/Au (100 nm), with dimensions 150 μm×150 μm, while the bottom Al electrode has a thickness of 100 nm. Tens of $Hf_{0.45}Zr_{0.55}O_{1.76}$ capacitors were fabricated in this manner, Figs. 1(c) and 1(d) presenting an optical image of several of these capacitors (top electrodes) and, respectively, the schematic cross-section of these devices.

The electrical characterization of MFS devices was performed between the top and the bottom electrode, which plays the role of ground electrode. All measurements were carried out using a Keithley SCS 4200 station with all channels connected to low noise amplifiers. The station is connected to a probe station, on which the chip containing all devices is placed. The entire probe station is enclosed in a Faraday cage. All experiments are performed inside the Faraday cage, which is closed during measurements. In order to check for hysteretic behavior of MFS devices, electrical characterizations were performed at various voltage sweeps. No fitting algorithms were applied during or after measurements. The yield was very good: 95% of the MFS capacitors showed similar capacitance-voltage (C-V) characteristics, within ±5% dispersion, while 5% of all devices had problems due to their metallic contacts, which were exfoliated during the positioning of the sharp metallic probe tips.

The typical C-V dependences, displayed in Fig. 2, demonstrate a hysteretic behavior, which have a counterclockwise trace, caused mainly by the interfacial layer formed during ALD deposition and located between the ferroelectric and the Si substrate [21,22]. This layer at the ferroelectric/semiconductor interface consists of residual impurities acting as slow states and related to hydroxyl groups formed during ALD growth from water. The hysteretic C-V dependences in Fig. 2 were recorded at 100 kHz, for different sweeping ranges indicated in the legend. As can be seen from the inset of this figure, the window (the width of the hysteresis

loop) increases initially with the sweeping range and then decreases, due to an increased number of charge carriers that tunnel through the very thin ferroelectric layer at larger applied voltages.

A typical DC current-voltage dependence of the MFS devices, for poling signals of opposite polarity, is shown in Fig. 3(a) and reveals the existence of two distinct conduction states of HfZrO devices, termed ON and OFF. The corresponding band diagrams of the MFS structures in the absence of an applied bias are represented in Fig. 3(b). As can be seen from this figure, the opposite poling signals, which define the ON and OFF states, cause an opposite orientation of the dipole in the ferroelectric layer, equivalent to a built-in field, which modifies the band diagram of the devices. Thus, the currents/resistances in the ON and OFF states are different, inducing the rectifying behavior. In order to obtain the current-voltage characteristic depicted in Fig. 3(a), we applied the following procedure: before measurement, a poling signal consisting of a ramp of +10 V was applied to the device for 20 s, and the I-V dependence was measured in the ON state (black line). Then, the same poling signal, with the same duration but reversed polarity (-10 V) was applied on the device, which was measured in the OFF state (red line). The procedure was applied several times for each device to see if the ON and OFF states are preserved, but no significant changes were detected. In order to identify the conduction mechanism in the MFS device, we fitted the experimental data with different formulas, corresponding to different mechanisms, the best fit being obtained for the Fowler-Nordheim tunneling, for which [23]:

$$I \propto E^2 \exp\left(\frac{-4\sqrt{2em}}{3\hbar E}\phi_b^{3/2}\right) \quad (1)$$

where E is the electric field, m the effective mass of electrons and ϕ_b the barrier height at the ferroelectric/Si interface. The fit is presented in the top inset of Fig. 3(a), the value of ϕ_b calculated from the slope of the fit (red line), for an electron effective mass in HfZrO of $0.47m_0$

[24], with m_0 the free electron mass, being about 0.3 V. The identified tunneling mechanism explains also the shape of the C-V curve corresponding to largest sweeping voltage employed, i.e of +/-5 V. More precisely, the decrease of the capacitance at large biases is caused by tunneling, more probable at high voltages, which decreases the charges contributing to the capacitive response.

The ratio of the ON and OFF currents (corresponding to poling signals of opposite polarities) is about 10^4, as can be seen from the bottom inset of Fig. 3(a), which represents the log(I)-V characteristics. The two dependences are drawn with the same line type as that used for the corresponding I-V characteristics.

3. Fabrication and characterization of an antenna array at 26 GHz and of an $Hf_{0.45}Zr_{0.55}O_{1.76}$ -based energy harvester

Because the currents of the rectifying HfZrO tunneling diodes are at mA level, the diodes can be coupled to an antenna array in order to harvest electromagnetic energy at 26 GHz (a bandwidth designated for Internet of Things-IoT). Therefore, we have also fabricated an antenna array at 26 GHz using optical lithography, measured it, and used its electromagnetic parameters to estimate the performance of the harvester when interconnected with the $Hf_{0.45}Zr_{0.55}O_{1.76}$ MFS device (see Fig. 4). The antenna array was fabricated on a SiO_2 substrate (300 nm thick) thermally deposited on 525-μm-thick high-resistivity silicon (HR Si). The metallization is a 500 nm thick gold layer. The width and length of an antenna patch are W = 2.22 mm and L = 1.46 mm, respectively, while the spacing between antennas is about $\lambda_0/2$ in the (x,y) directions, with λ_0 the free-space wavelength. In our case, $\lambda_0 \approx 11.54$ mm at 26 GHz. The reference antenna input impedance is 50 Ω.

We have measured the antenna return loss ($|S_{11}|$) and the imaginary part of its input impedance, the results being shown in Figs. 5(a) and 5(b), respectively. From the first figure it follows that the best matching to 50 Ω occurs at 25.9 GHz from simulations, while it is found at

27.8 GHz from measurements. The difference between simulated and measured $|S_{11}|$ values is explained by the large difference between the thickness of the antenna array (of 500 μm) and the free space wavelength (about 20 times larger, i.e. 1.15 cm at 26 GHz). Due to this fact, the antenna array does not radiate only above the radiation plane, represented by the antenna patches, but also below it, and the radiation efficiency is reduced. Therefore, during measurements the antenna array was mounted on a metallic support (not considered in simulations due to the very large computational time needed), to reduce the unwanted reflections and to increase its radiation efficiency. Nevertheless, the simulated and measured resonances (for which the imaginary part of the antenna input impedance is equal to zero) are very closely spaced, i.e. at 25.66 GHz from simulations and 25.14 GHz from measurements.

To demonstrate the possibility of using MFS devices coupled to antenna arrays as electromagnetic energy harvesters, we integrated the MFS device in a coplanar (CPW) waveguide connected to the antenna array via a CPW taper. The output of the CPW MFS is further connected, by another CPW taper, to an optimized load R = 280 Ω in parallel with C = 5 pF (see Fig. 6). Using the AWR simulator, in which we introduced the experimental I-V data, we further estimated the time domain response of the harvester (see Fig. 7) at various microwave voltages. The responsivity and NEP at various microwave voltages is displayed in Fig. 8. For an incident power between -20 dBm and 10 dBm, the responsivity is in the 63.34-0.47 V/W range, whereas the NEP spans the range 3.84-514.46 nW/Hz$^{0.5}$. A comparison of our rectenna (i.e. the antenna array integrated with the HfZrO diode) with other existing rectennas in terms of the performance for harvesting millimeter waves working in the same bandwidth is difficult since the conversion efficiency defined as $\eta = P_{DC} / P_{RF}[\%]$ is generally calculated at various frequencies and various load resistances. Here P_{DC} is the DC power, while P_{RF} is the input RF power at a given frequency. However, considering the RF power as 0 dBm (10 mW) we obtain an efficiency of 6% at 26 GHz, while 10% efficiency is obtained at the same RF power at 24 GHz with a rectifier consisting of a commercial Schottky diode [25].

4. Conclusions

In this paper, HfZrO ferroelectrics with a thickness of 6 nm were grown directly on Si using atomic layer deposition, top and bottom metallic electrodes being subsequently deposited by electron-beam metallization techniques. Depending on the polarity of the ±10 V poling voltages, the current-voltage dependence of these HfZrO tunneling diodes shows a rectifying behavior for different polarizations, the ON-OFF ratio being about 10^4 and the currents having large values, of mA level. We have demonstrated that, by using a metal-ferroelectric-semiconductor device coupled to an antenna array, we can collect electromagnetic energy at 26 GHz, with a responsivity of 63 V/W and a NEP of 4 nW/Hz$^{0.5}$, high enough to feed things with a very low power consumption connected in an IoT network. For example, processors for sensing applications as in IoT consume only 35 pW in the standby mode, and 290 nW in the active mode [26]. Such types of extremely complex low-power circuits can be fed wirelessly by the harvester proposed in this work. In fact, many other things in an IoT besides sensors could be fed in the same way, since the required active power levels are fractions of μW [27].

Acknowledgments:

The authors would like to thanks Prof. Marco Farina, Dr. Andreea Di Donato and Dr. Eleonora Pavoni from Università Politecnica delle Marche, Ancona, Italy for performing the Piezoresponse Force Microscopy measurements on our samples.

Some of the authors (MD, MA, AD and DD) acknowledge the financial support of project number PN-III-P4-ID-PCCF-2016-0033.

References

[1] D. Martin, J. Müller, T. Schenk, T. M. Arruda, A. Kumar, E. Strelcov, E. Yurchuk, S. Müller, D. Pohl, U. Schröder, S. V. Kalinin, and T. Mikolajick, Ferroelectricity in Si-doped HfO_2 revealed: a binary lead-free ferroelectric, Adv. Mater. 26, 8198-8202 (2014).

[2] Z. Fan, J. Chen, and J. Wang, Ferroelectric HfO_2-based materials for next generation ferroelectric memories, J. Advanced Dielectrics 6, 1630003 (2016).

[3] M. Si, C.-J. Su, C. Jiang, N. J. Conrad, H. Zhou, K. D. Maize, G. Qiu, C.-T. Wu, A. Shakouri, M. A. Alam, and P. D. Ye, Steep-slope hysteresis-free negative capacitance MoS_2 transistors, Nature Nanotechnology 13, 24-28 (2018).

[4] E. Ko, H. Lee, Y. Goh, S. Jeon, and C. Shin, Sub-60-mV/decade negative capacitance FinFET with sub-10-nm hafnium-based ferroelectric capacitor, IEEE J. Electron Devices Society 5, 306-309 (2017).

[5] A. I. Khan, M. Hoffmann, K. Chatterjee, Z. Lu, R. Xu, C. Serrao, S. Smith, L. W. Martin, C. Hu, R. Ramesh, and S. Salahuddin, Differential voltage amplification from ferroelectric negative capacitance, Appl. Phys. Lett. 111, 253501 (2017).

[6] M. Dragoman, M. Aldrigo, M. Modreanu, and D. Dragoman, Extraordinary tunability of high frequency devices using $Hf_{0.3}Zr_{0.7}O_2$ ferroelectric at very low applied voltages, Appl. Phys. Lett. 110, 103104 (2017).

[7] M. Dragoman, M. Modreanu, I. M. Povey, S. Iordanescu, M. Aldrigo, C. Romanitan, D. Vasilache, A. Dinescu, and D. Dragoman, Very large phase shift of microwave signals in a $Hf_xZr_{1-x}O_2$ ferroelectric at ±3V, Nanotechnology 28, 38LT04 (2017).

[8] M. Dragoman, M. Modreanu, I. Povey, S. Iordanescu, M. Aldrigo, A. Dinescu, D. Vasilache, C. Romanitan, 2.55 GHz miniaturised phased antenna array based on 7 nm-thick $Hf_xZr_{1-x}O_2$ ferroelectrics, Electronics Letters (2018), doi: 10.1049/el.2018.0111.

[9] V. Garcia and M. Bibes, Ferroelectric tunnel junctions for information storage and processing, Nature Commun. 5, 4289 (2014).

[10] E. W. Cowell III, N. Alimardani, C. C. Knutson, J. F. Conley Jr., D. A. Keszler, B. J. Gibbons, and J. F. Wager, Advancing MIM electronics: amorphous metal electrodes, Advanced Materials 23, 74-78 (2011).

[11] A. Chanthbouala, A. Crassous, V. Garcia, K. Bouzehouane, S. Fusil, X. Moya, J. Allibe, B. Dlubak, J. Grollier, S. Xavier, C. Deranlot, A. Moshar, R. Proksch, N. D. Mathur, M. Bibes, and A. Barthelemy, Solid-state memories based on ferroelectric tunnel junctions, Nature Nanotechnology 7, 101-104 (2012).

[12] W. J. Hu, Z. Wang, W. Yu, and T. Wu, Optically controlled electroresistance and electrically controlled photovoltage in ferroelectric tunnel junctions, Nature Commun. 7, 10808 (2016).

[13] Z. Xi, J. Ruan, C. Li, C. Zheng, Z. Wen, J. Dai, A. Li, and D. Wu, Giant tunnelling electroresistance in metal/ferroelectric/semiconductor tunnel junctions by engineering the Schottky barrier, Nature Commun. 8, 15217 (2017).

[14] G. Moddel, S. Grover, *Rectenna Solar Cells*, Springer, New York (2013).

[15] J. Wang, Se. S. Mottaghian, and M. F. Barough, Passivation properties of atomic-layer-deposited hafnium and aluminum oxides on Si surfaces, IEEE Trans. Electron Dev. 59, 342-348, 2012.

[16] J. C. Vandana, N. Batra, J. Panigrahi, R. Singh, K. K. Maurya, R. Srivastava, P. K. Singh, Silicon surface passivation using thin HfO_2 films by atomic layer deposition, Applied Surface Science 357, 635-642 (2015).

[17] M. Modreanu, J. Sancho-Parramon, O. Durand, B. Servet, M. Stchakovsky, C. Eypert, C. Naudin, A. Knowles, F. Bridou, and M.-F. Ravet, Investigation of thermal annealing effects on microstructural and optical properties of HfO_2 thin films, Appl. Surf. Sci. 253, 328-334 (2006).

[18] Supporting Information

[19] A. Chernikova, M. Kozodaev, A. Markeev, D. Negrov, M. Spiridonov, S. Zarubin, O. Bak, P. Buragohain, H. Lu, E. Suvorova, A. Gruverman and A. Zenkevich, Ultrathin $Hf_{0.5}Zr_{0.5}O_2$ ferroelectric films on Si, ACS Applied Materials & Interfaces 8, 7232–7237 (2016).

[20] A. Tselev, P. Yu, Y. Cao, L. R. Dedon, L. W. Martin, S. V. Kalinin and P. Maksymovych, Microwave a.c. conductivity of domain walls in ferroelectric thin films, Nature Communications 7, 11630 (2016).

[21] H. García, H. Castán, S. Dueñas, L. Bailón, F. Campabadal, O. Beldarrain, M. Zabala, M. Bagallo González, and J. M. Rafí, Electrical characterization of atomic-layer-deposited hafnium oxide films from hafnium tetrakis(dimethylamide) and water/ozone: Effects of growth temperature, oxygen source, and postdeposition annealing, J. Vac. Sci. Technol. A 31, 01A127 (2013).

[22] Y. W. Kim, Y. Roh, J.-B. Yoo, and H. Kim, Characteristics of atomic layer deposition grown HfO_2 films after exposure to plasma treatments, Thin Solid Films 515, 2984-2989 (2007).

[23] E. W. Lim and R. Ismail, Conduction mechanism of valence change resistive switching memory: a survey, Electronics 4, 586-613 (2015).

[24] Z. Dong, X. Cao, T. Wu, and J. Guo, Tunneling current in HfO2 and Hf0.5Zr0.5O2-based ferroelectric tunnel junction, J. Appl. Phys. 123, 094501 (2018).

[25] S. Daskalakis, J. Kimionis, J. Hester, A. Collado, Manos M. Tentzeris, and A. Georgiadis, Inkjet printed 24 GHz rectenna on paper for millimeter wave identification and wireless power transfer applications, 2017 IEEE MTT-S International Microwave Workshop Series on Advanced Materials and Processes for RF and THz Applications (IMWS-AMP) (2017), pp. 1-3, 20-22 September 2017, Pavia, Italy

[26] S. Hanson, M. Seok, Y.-S. Lin, Z. Y. Foo, D. Kim, Y. Lee, N. Liu, D. Sylvester, and D. Blaauw, A low-voltage processor for sensing applications with picowatt standby mode, IEEE J. Solid-State Circuits 44, 145-154 (2009).

[27] H. Jayakumar, K. Lee, W. S. Lee, A. Raha, Y. Kim, and V. Raghunathan, Powering the internet of things, Proceedings of the 2014 International Symposium on Low Power Electronics and Design, ISLPED '14, 2014. doi: 10.1145/2627369.2631644.

Figure captions

Fig. 1 (a) Surface morphology and phase image (b) of the $Hf_{0.45}Zr_{0.55}O_{1.76}$ thin film obtained by applying sequentially a bias of +2/-2 V during the scan. The bright stripes in (b) were obtained with +2 V and the dark stripes with -2 V; (c) Optical image of top electrodes of $Hf_{0.45}Zr_{0.55}O_{1.76}$ capacitors, and (d) schematic of the cross-section of the MFS device.

Fig. 2 C-V dependence of the MFS device at 100 kHz, for different sweeping ranges. Inset: Dependence of the windows of C-V curves on the sweeping range.

Fig. 3 (a) DC I-V dependence of the MFS device. Top inset: Fitting of I-V data with Fowler-Nordheim tunneling mechanism. Bottom inset: I-V dependence in a semi-log representation, with the same line style. (b) Band diagrams for the ON and OFF states in the absence of an applied bias

Fig. 4 Optical image of the antenna array at 26 GHz.

Fig. 5 (a) Return loss $|S_{11}|$ of the antenna array, and (b) imaginary part of its input impedance.

Fig. 6 Circuit layout of the harvester.

Fig. 7 Time domain response of the harvester.

Fig. 8 Predicted responsivity and NEP of the harvester at 26 GHz for different input powers.

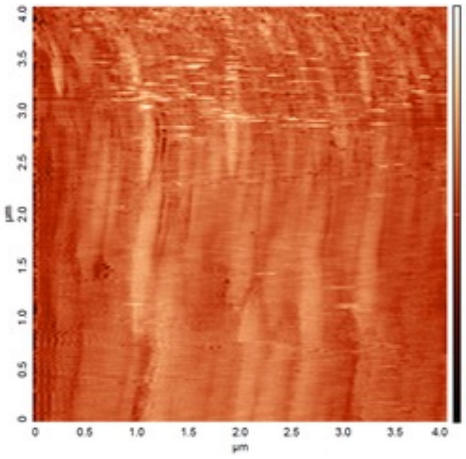

(a)

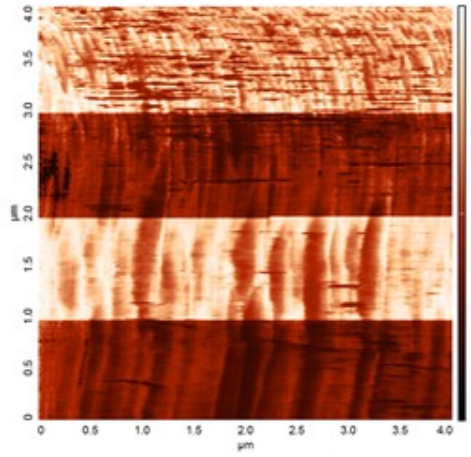

(b)

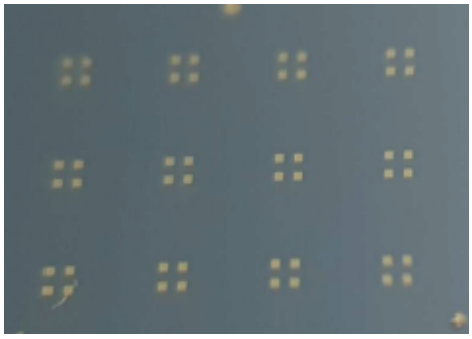

(c)

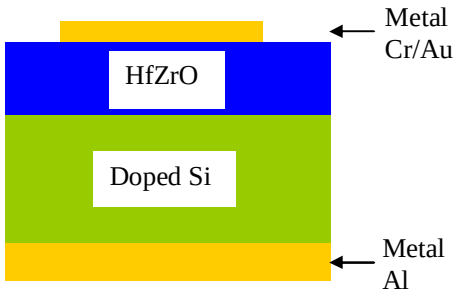

(d)

Fig. 1

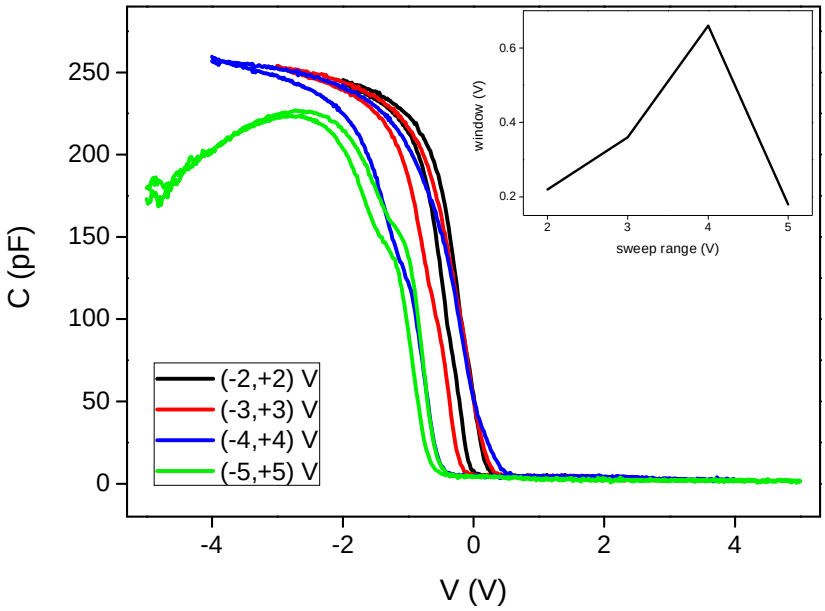

Fig. 2

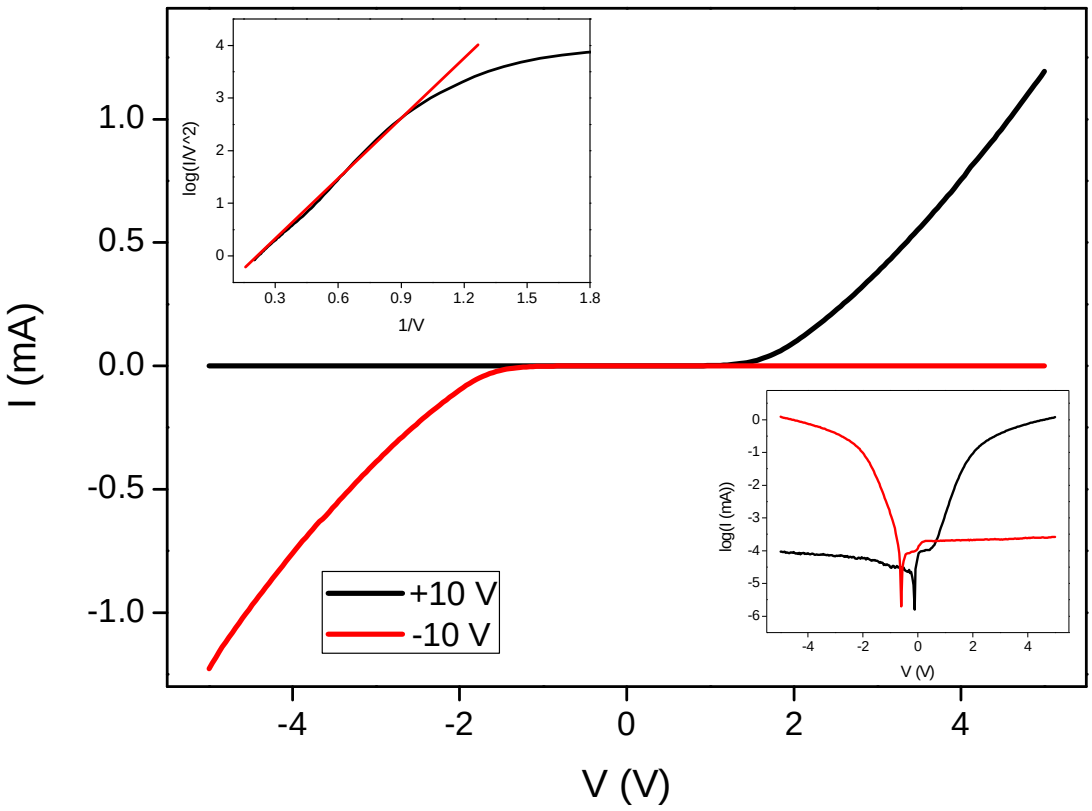
I (mA)
V (V)
+10 V
-10 V
log(I/V^2)
1/V
log(I (mA))
V (V)

(a)

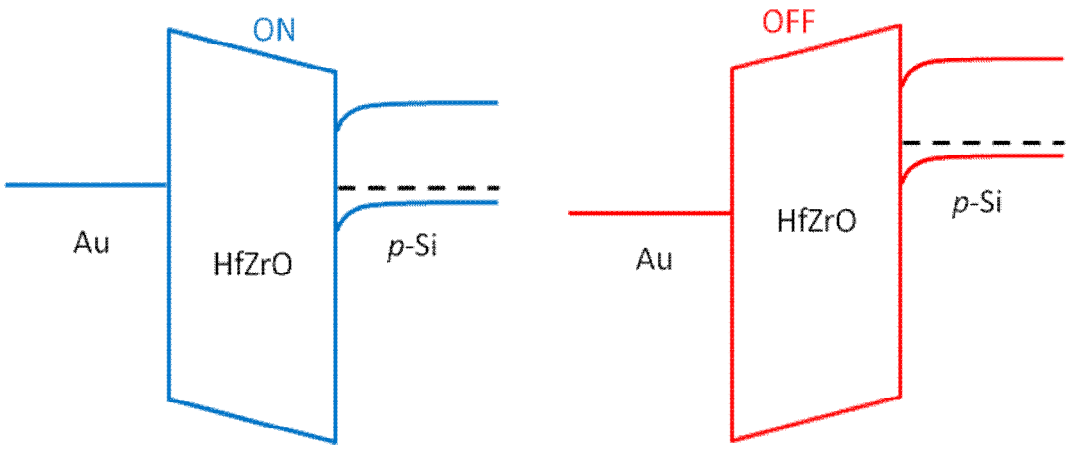
ON
Au
HfZrO
p-Si
OFF
Au
HfZrO
p-Si

(b)

Fig. 3

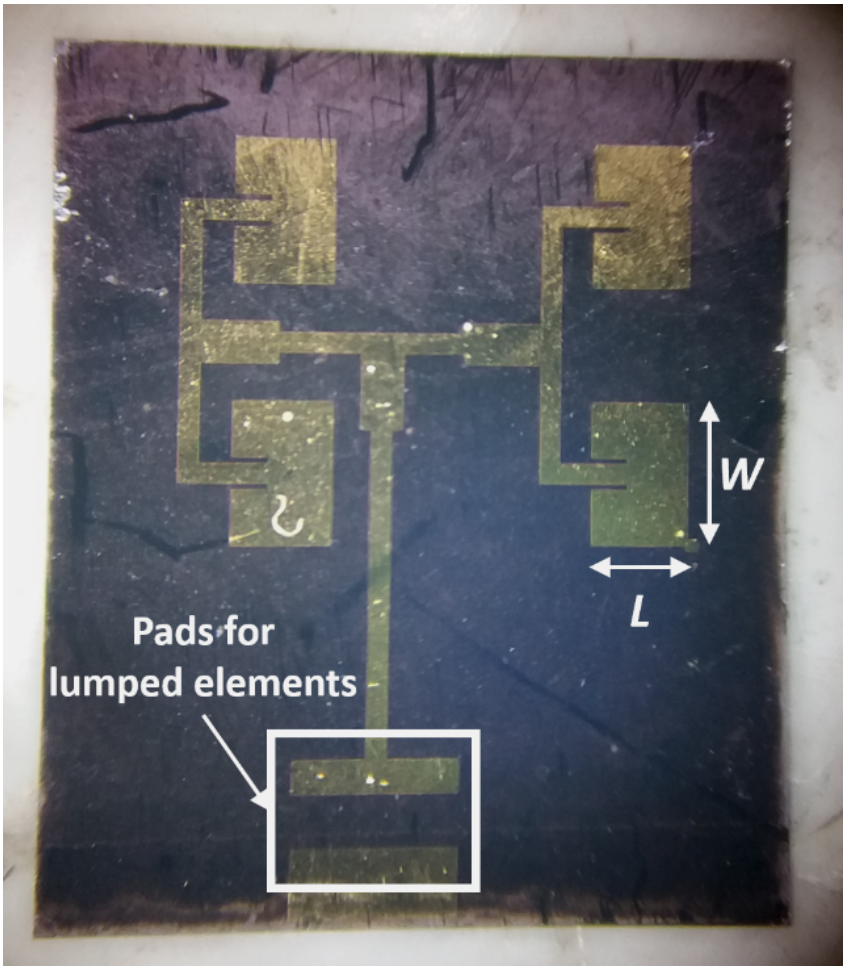

Fig. 4

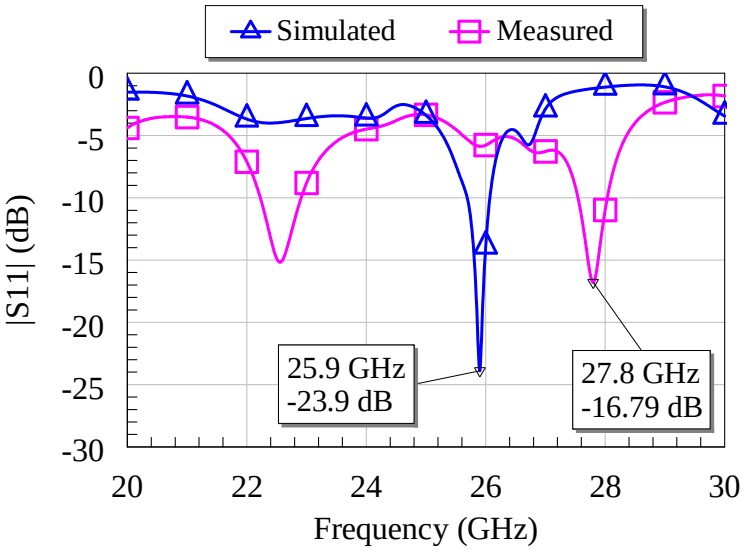
Simulated
Measured
|S11| (dB)
0
-5
-10
-15
-20
-25
-30
25.9 GHz
-23.9 dB
27.8 GHz
-16.79 dB
20
22
24
26
28
30
Frequency (GHz)

(a)

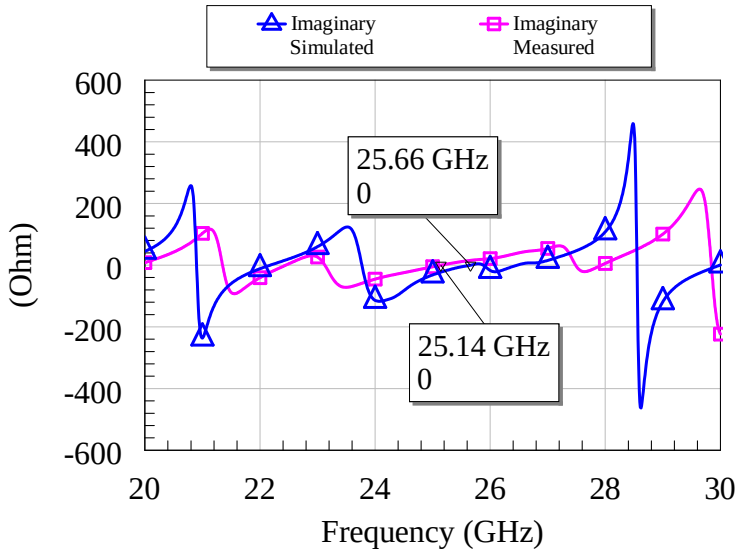
Imaginary
Simulated
Imaginary
Measured
(Ohm)
600
400
200
0
-200
-400
-600
25.66 GHz
0
25.14 GHz
0
20
22
24
26
28
30
Frequency (GHz)

(b)

Fig. 5

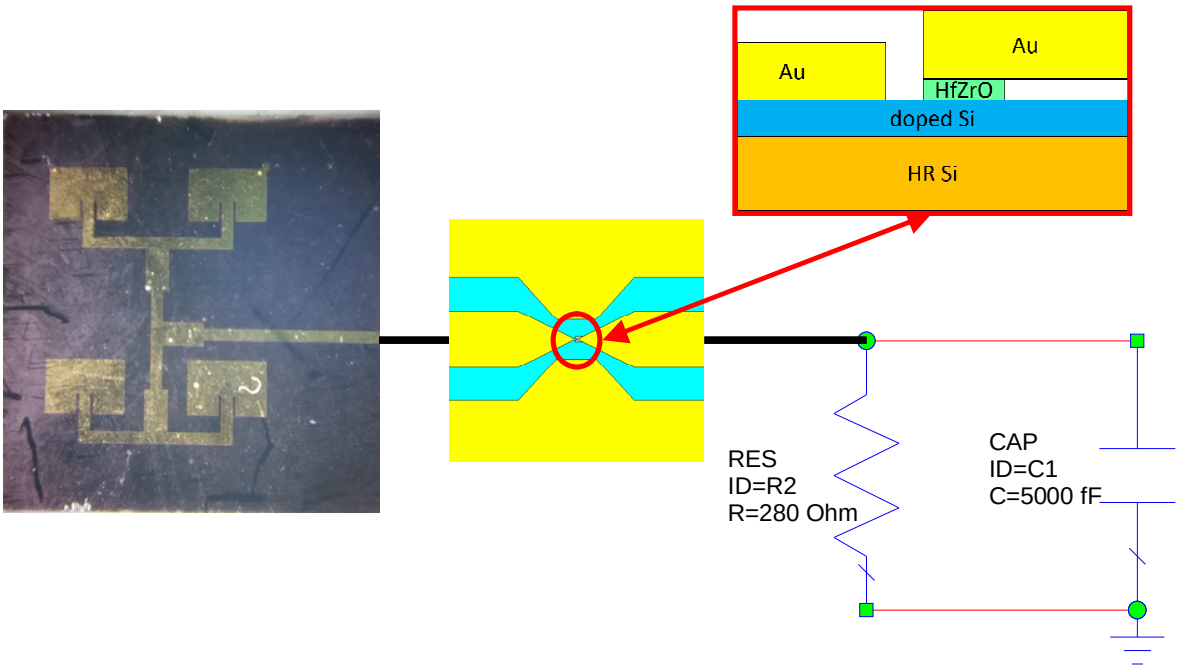

Fig. 6

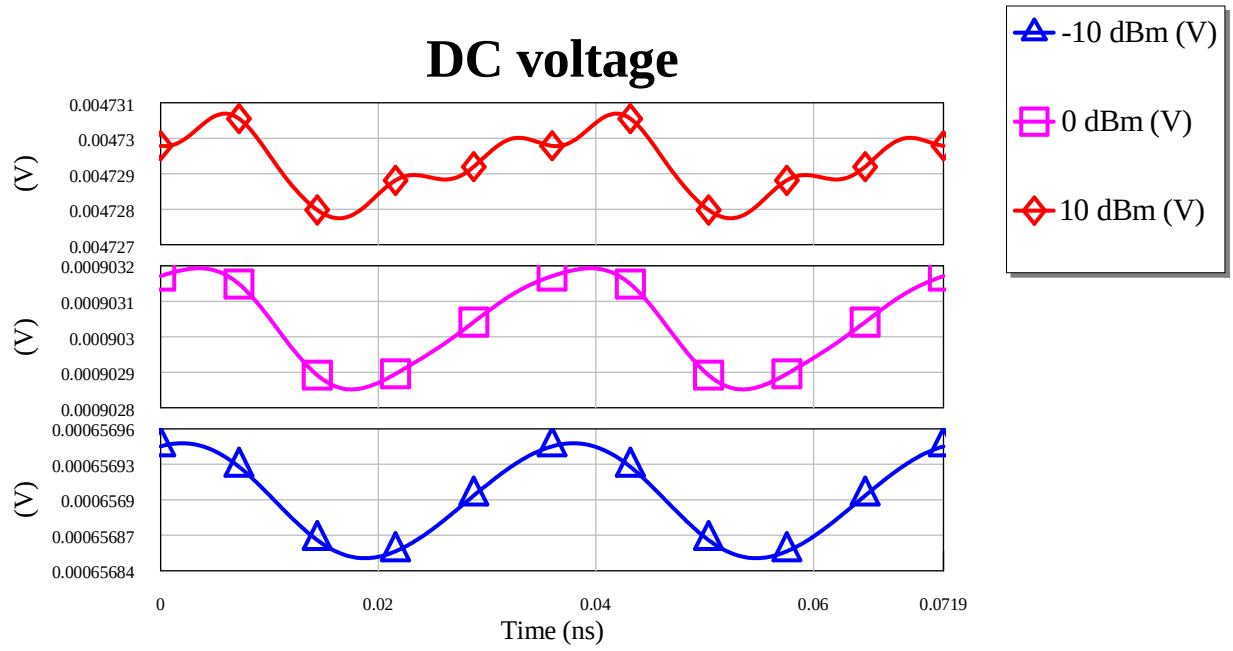
DC voltage
-10 dBm (V)
0 dBm (V)
10 dBm (V)
(V)
0.004731
0.00473
0.004729
0.004728
0.004727
0.0009032
0.0009031
0.000903
0.0009029
0.0009028
0.00065696
0.00065693
0.0006569
0.00065687
0.00065684
0
0.02
0.04
0.06
0.0719
Time (ns)

Fig. 7

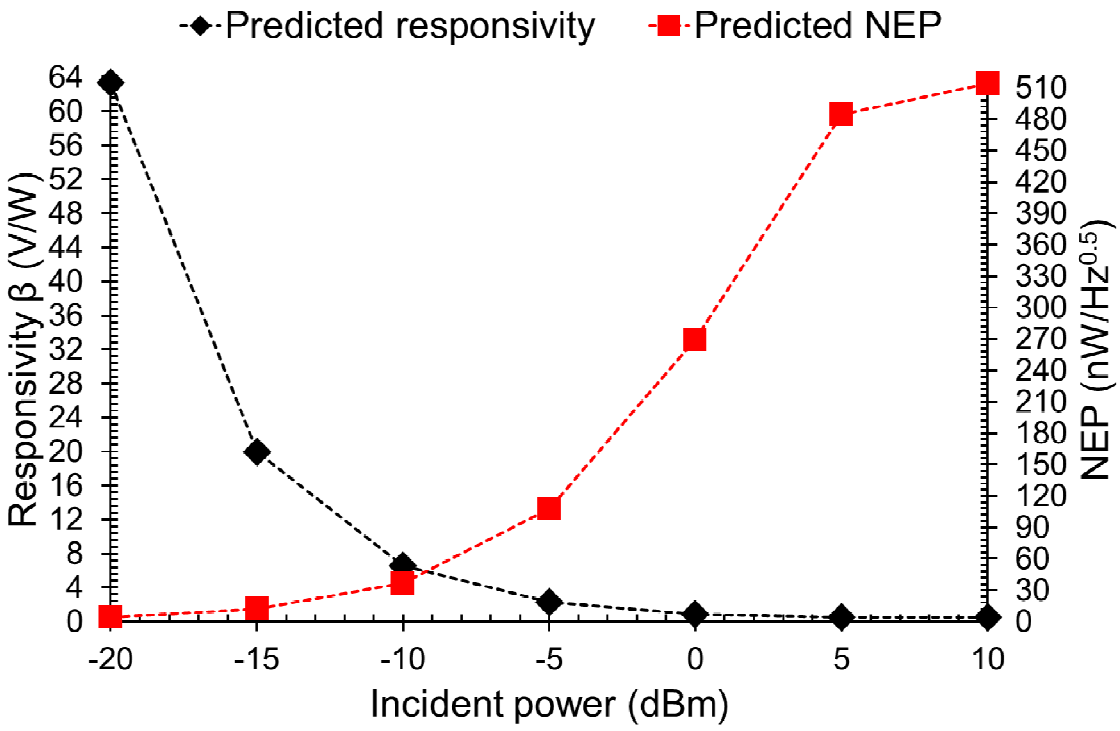
Predicted responsivity
Predicted NEP
Responsivity β (V/W)
NEP (nW/Hz^0.5)
Incident power (dBm)
64
60
56
52
48
44
40
36
32
28
24
20
16
12
8
4
0
510
480
450
420
390
360
330
300
270
240
210
180
150
120
90
60
30
0
-20
-15
-10
-5
0
5
10

Fig. 8